Extreme Frequency Conversion from Soliton Resonant Interactions

Myungwon Hwang and Andres F. Arrieta*
School of Mechanical Engineering, Purdue University, West Lafayette, Indiana 47907, USA

(Received 14 June 2020; accepted 27 January 2021; published 19 February 2021)

We present a metastructure architecture with a bistable microstructure that enables extreme broadband frequency conversion. We use numerical and experimental tools to unveil the relationship between input excitations at the unit cell level and output responses at the macrostructural level. We identify soliton-lattice mode resonances resulting in input-independent energy transfer into desired metabeam vibration modes as long as transition waves are triggered within the metastructure. We observe both low-to-high and high-to-low incommensurate frequency interactions in the metabeams, thus enabling energy exchange between bands 2 orders of magnitude apart. This behavior generalizes fluxon-cavity mode resonance in superconducting electronics, providing a general method to extreme frequency conversion in mechanics. Importantly, the introduced architecture allows for expanding the metamaterials design paradigm by fundamentally breaking the dependence of macroscopic dynamics on the unit cell properties. The resulting input-independent nature implies potential applications in broadband frequency regulation and energy transduction.

DOI: 10.1103/PhysRevLett.126.073902

Introduction.—Solitary waves appear in various physical systems [1] playing a pivotal role in applications, including waveguiding [2], photonics [3], optical communications [4], reversible logic gates [5], lasing [6], morphing structures [7], nondestructive testing [8], and soft robotics [9]. A unique aspect of solitons is their quasiparticle characteristics. This allows for better imaging using sonic bullets [10] or dense wavelength-division multiplexing for optical communications exploiting cavity solitons [11]. Solitons' resonant interactions with cavities have enabled the generation of lasers exhibiting frequency conversion not readily available with conventional sources exploiting fluxons—a type of transition wave or topological soliton—in Josephson junctions [12]. Such extreme frequency conversion in mechanical systems is less common and is typically achieved via subharmonic, superharmonic, or combination resonances [13] and nonlinear coupling between normal modes [14]. Nonlinear multimode metamaterials can provide alternate ways to attain frequency conversion through their amplitude-dependent dispersion relations [15,16]. Intermodal interactions through nonlinearly generated higher harmonics have been theoretically and experimentally demonstrated, enabling energy exchange between different wave modes [17–19]. Furthermore, magnetic metamaterials featuring engineered defects have demonstrated conversion from high- to low-frequency modes through resonant coupling between localized defect modes and extended lattice modes [20]. However, to excite these interaction mechanisms, the defect mode's frequency needs to be commensurate with or a combination of the system's modes, still limiting the attainable frequency bandwidth.

Lattices composed of bistable elements can support transition waves exhibiting particlelike behavior [21–23]. When the constitutive on-site members are built with asymmetric bistable elements, transition waves become unidirectional [24,25] and exhibit unique input-independent dynamics [26], implying strong potential for broadband applications. Enabling nonlinear interactions similar to fluxon-cavity mode resonances exploiting the input frequency independence of transition waves offers the potential for extreme energy conversion currently absent in mechanical systems. In this study, we demonstrate extreme energy exchange in mechanical systems with metabeams composed of a bistable microstructure that promotes nonlinear coupling between wave and metastructural modes in an analogous process to fluxons interacting with cavity modes in superconductors [6,12]. Importantly, the soliton resonant interactions enable extreme frequency conversion and response manipulation in mechanical systems, without recourse to dispersion-related phenomena. The unveiled dynamics are insensitive to the excitation frequency, thus laying the foundation for a new physical mechanism, the dynamics of which are independent of the metamaterial building block size.

Experimental results.—To illustrate the extreme frequency conversion phenomenon, we manufacture and test

a metabeam featuring an engineered bistable microstructure. The model metabeam is built by 3D printing a ladderlike structure [black component in Fig. 1(a)], the rungs of which are interconnected by springlike features providing intersite interaction. The intersite members are aligned at a small offset distance from the metabeam's center line. This design feature is introduced to break the cross section's symmetry about the center line, allowing the excitation of the bending modes by in-plane inputs (see Movie S1 [27]). The metabeam is then fitted between a set of flexible holders [white components in Fig. 1(a)], providing flexibility in the transverse direction and allowing the microstructure to exhibit two different stable states [red and green dashed lines in Figs. 1(a)(i) and 1(a)(ii)]. In this example setup, one end of the structure is clamped to realize a fixed-free boundary condition. A harmonic displacement input is imposed at the first element in the in-plane direction through an electrodynamic shaker. The input and output displacements are measured by a set of laser displacement sensors, pointing at the flat surfaces of the shaker head and near the free end of the structure, respectively. The overall experimental setup is shown in Fig. 1(a)(iii), and more detailed fabrication and experimental methods are given in Sec. 1 of Supplemental Material [27].

To summarize the input and output frequency relations, we construct an *output frequency diagram* [Figs. 1(b) and 1(c)]. The diagram summarizes up to the 20 largest peaks of the output displacement's power spectral density (DPSD) as a function of the input frequency. Each dot in the diagram represents the available frequency component of the output response, while its size indicates the relative intensity: A larger dot indicates larger spectral contribution. For each input cases, the relative intensity r_{DPSD} is calculated by $\mathrm{DPSD}_i/\mathrm{DPSD}_{\mathrm{max}}$, where DPSD_i is the power of the ith frequency component and $\mathrm{DPSD}_{\mathrm{max}}$ is the power of the most dominant peak. DPSD_i's less than 0.1% of $\mathrm{DPSD}_{\mathrm{max}}$ are discarded to declutter the output frequency diagrams. For better visualization of the subdominant frequency peaks, the dots are logarithmically scaled such that they appear as $2^{\log_{10} r_{\mathrm{DPSD}}}$ in size. Blue dots indicate the generation of in-plane transition waves within the metabeam, while red dots represent responses involving no phase transitions. The DPSD is obtained when the system attains steady state with the aid of welch function in PYTHON's scipy library at 1000 Hz sampling frequency without windowing.

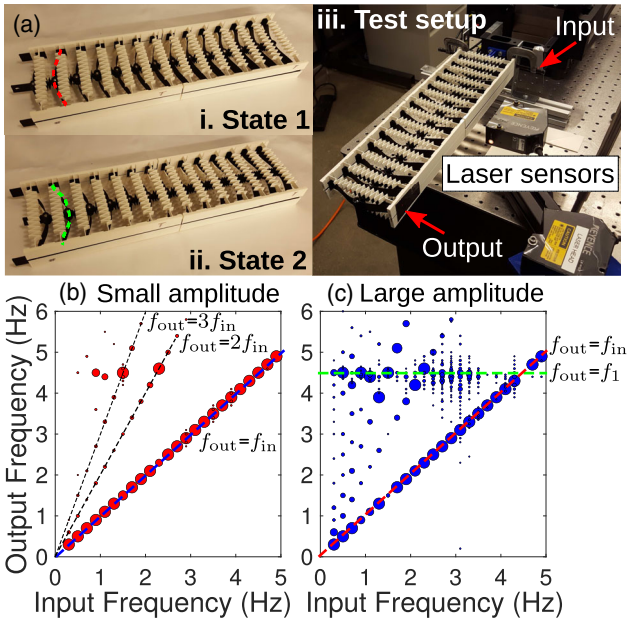

FIG. 1. (a) Experimental demonstrator and shaker test setup. Experimental output frequency diagrams under (b) small- and (c) large-amplitude excitations. f_{out}, f_{in}, and f_1 are the output frequency, input frequency, and fundamental mode of the metabeam, respectively.

For a relatively small input displacement about one of the stable states for which transition waves are not triggered, the dominant output frequency corresponds to either the input frequency or its harmonics close to the fundamental mode (4.62 Hz [27]) of the metabeam [Fig. 1(b)]. The harmonic contributions' appearance is due to the experimental limitation in generating purely sinusoidal displacement signals with our test setup, leading excitation of superharmonics of the input frequency (Sec. 2 of Supplemental Material [27]). In this low forcing amplitude regime, the observed dynamics are fully accountable in terms of the typical linear and weakly nonlinear responses that do not involve the triggering of transition waves.

Increasing the imposed displacement amplitude further triggers transition waves, revealing an output frequency branch close to the structural mode [green dashed line in Fig. 1(c) and Movie S2] in addition to a branch corresponding to the input frequencies (red dashed line). Interestingly for the input frequencies above 2.5 Hz, the frequencies of this subdominant output branch are not the results of superharmonic resonance [see the spectral content around 4.5 Hz in Figs. S2(e) and S2(f)]; rather, these exhibit incommensurate relations with the input frequencies. Our experiments thus reveal that the generation of transition waves results in a solution branch showing coherent output frequency around the fundamental mode f_1 of the metabeam unrelated to the input frequencies. Notably, the transition wave generation yields a fundamental mechanism to achieve incommensurate frequency resonance displaying strong stability, which is uncommon in structural systems [30]. As this dynamics manifests when transition waves (i.e., topological solitons) are triggered, we referred to this phenomenon as *solitonic resonance*.

The solitonic resonance can be explained by the transition wave's particlelike nature [1,31]. In this regime, the generated quasiparticles impulsively excite the metastructure continuously. This triggers lasting transients even

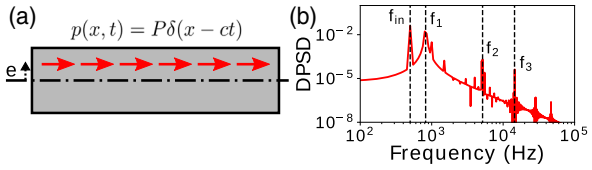

FIG. 2. (a) Schematic representation of a beam subjected to a moving particle. (b) Power spectral density of the approximated tip displacement of the beam in a fixed-free configuration.

in a nonconservative system. This mechanism is similar to frequency up-conversion in devices [32], but our metabeam utilizes the quasiparticle motion instead of direct impacts. We can further analogize the metabeam's solitonic resonance employing an Euler-Bernoulli beam subjected to an in-plane traveling particle. The motion of a single particle moving along the beam's length can be mathematically represented as a localized traveling impulse [Fig. 2(a)]. This beam problem can be solved exactly by a modal expansion method (see Sec. 4 of Supplemental Material [27] for the analysis details). An example five-term approximation of the tip displacement for such a beam in a fixed-free configuration is obtained by sending 22 particles every 2 ms. The resulting DPSD obtained for the response between 24 and 44 ms [Fig. 2(b)] confirms that a moving impulse indeed excites the normal modes f_n's of the beams.

Numerical results.—Although the postbuckled beam design as the microstructure readily yields bistability in an experimental demonstrator, a spring-joined bistable unit cell design is more advantageous for a simpler mathematical description. Thus, we adopt it in the subsequent numerical investigation by constructing a beamlike frame with underlying spring-mass bistable microstructures [23]. We introduce an offset from the center line of the frame [dash-dotted line in Fig. 3(a)] to break the system's cross-sectional symmetry and amplify the flexural motion. The buckled beam, providing the local bistability, is idealized by a pair of linear springs with the constants k_2 and k_3. The spring with the constant k_1 serves as the intersite connection between neighboring on-site members. The flanges and the holders of the experimental demonstrator form an external elastic frame, which is idealized by the rest of the linear springs (k_4–k_8) in the mathematical design. Additionally, small mass proportional damping is imposed across the metabeam to suppress any unwanted transient effects.

A fixed-free boundary condition is used; however, the ensuing dynamics are independent of the boundary conditions (Sec. 6 of Supplemental Material [27]). Harmonic displacement input $u_1(t) = R - A\cos(2\pi f_{\text{in}} t - \phi_0)$ or force input $p(t) = F \sin 2\pi f_{\text{in}} t$ are used to separately excite the metabeam [33]. The excitation is applied in the in-plane direction at the leftmost node of the internal bistable lattice, where A, ϕ_0, and F are the displacement amplitude, phase constant, and forcing amplitude, respectively. The output displacement is measured at the top rightmost node in the out-of-plane direction. See Fig. 3(a) and Sec. 5 of Supplemental Material [27] for the full metabeam description and design parameters. The metabeam's dynamics are simulated using ABAQUS/STANDARD implicit nonlinear solver and reported in *output frequency diagrams*.

We first construct a numerical model qualitatively similar to the experimental metabeam, which is achieved by matching the unit cell natural frequency and the fundamental macrostructural mode of the numerical model to those of the experimental metabeam (see Supplemental Material [27] for the design parameters). The simulated output response diagrams display qualitative agreement with the experimental response. The metabeam under 1 mm input amplitude shows purely linear behavior, confirming that the solitonic resonance is not a product of the peculiar unit cell design [Fig. 3(b)]. Under 9.5 mm input amplitude, transition waves are triggered within the metabeam, resulting in coexisting linear and solitonic resonance solution branches [red and green dashed lines in Fig. 3(c)]. The numerical simulations for this case are then extended to a higher input frequency range, still showing the output frequency branch concentrated at ~4.62 Hz [34] but almost eliminating the branch corresponding to the input frequencies. This disappearance of the input frequency contribution is due to the aperiodic generation of the transition waves. At low input frequencies, such that the snap-through transitions at the excitation site occur at a much slower rate than the transition wave's propagation speed, each unit's interwell oscillation takes place at the same frequency as the input frequency, resulting in the direct contribution from the input. In contrast, increasing the input frequency

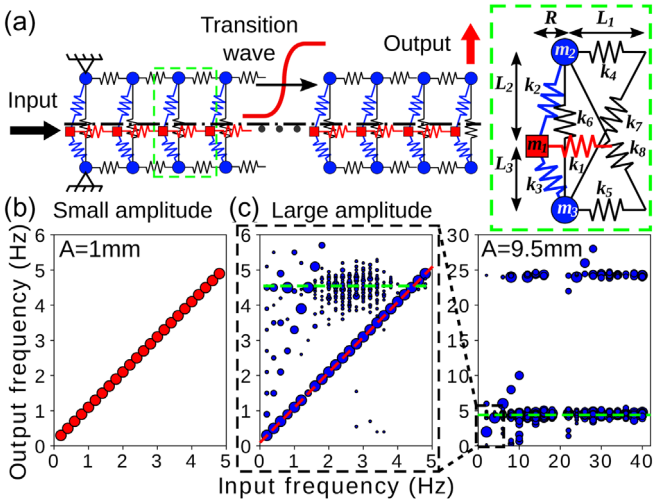

FIG. 3. (a) Schematic representation of the metabeam. Output frequency diagrams for a qualitatively similar numerical design under (b) small- and (c) large-amplitude excitations. The enlarged region shows the low-frequency responses corresponding to the experimental range.

results in a faster transition wave generation rate so that the newly generated and previously traveling transition waves interact with one another. Thereby, the resulting interwell oscillations occur at nondefinite rates, imposing the prevalence of transient effects in the response. The transient effect's dominance over the input frequency effect can be further manipulated by the system damping as long as manufacturing technology allows (Sec. 7 of Supplemental Material [27]).

Even more extreme energy transfer can be achieved, employing the force input, since the induced snap-through instability is chaotic in nature [35], hence facilitating the aperiodic generation of transition waves. As a baseline design, the spring constants are tuned to have the fundamental macroscopic mode at 26.3 Hz and the unit cell mode at 39.7 Hz (see Supplemental Material [27] for the design parameters). Transition waves can be excited via quasistatic or dynamic inputs but are more easily triggered by harmonic excitations around the unit cell mode, as shown in the response map [Fig. 4(a)]. The map indicates whether transition waves are generated for the given input amplitude and frequency combinations. Furthermore, the frequency range expands with increasing forcing amplitudes.

The particlelike nature of the transition waves can be clearly identified by the stable propagation of the kink-shaped waveform in Fig. 4(b)(i), showing the in-plane displacement u_1 of the center mass in the space configuration under a quasistatic (1 Hz) input. For higher input frequencies [36 Hz in Fig. 4(b)(ii)], the waveform is distorted by nonlinear interactions with other lattice modes. Nevertheless, the waveform starting at one stable state and ending at another is readily identifiable. In addition, the induced transition waves provoke response amplification as in mechanical resonance. Figure 4(c) shows the responses just below and above the forcing amplitude triggering transition waves. With only ~3.4% increase in the forcing amplitude, the output displacement w_2 amplifies as much as ~14 times (Sec. 8 of Supplemental Material [27]).

Figure 4(d)(i) shows the output frequency diagram for the baseline design under $F = 1$ N, and one representative response ($f_{\text{in}} = 36$ Hz) when transition waves are generated is given in Fig. 4(e). The resulting power spectral densities of w_2's again confirm that the generation of transition waves excites the macroscopic metastructure's fundamental mode [dashed line in Fig. 4(d)(i)]. Compared to the displacement input cases, however, almost complete energy transfer into this macroscopic mode can be achieved due to the aperiodic generation of transition waves, illustrated by the nondefinite state transition rates of the in-plane displacement u_1 at the excitation site [Fig. 4(e)(i)]. The effect of the generation rate disperses in the frequency spectrum, leaving the transient effect to dominate the out-of-plane response. As the forcing amplitude increases to 1.7 N, the input bandwidth yielding solitonic resonance broadens [Fig. 4(d)(ii) and Movie S3]. It is further observed that even noisy input sources can be transformed into a single coherent response mode (Sec. 9 of Supplemental Material [27]). Thus, the strongly nonlinear dynamics displayed by the proposed metastructures enable a robust mechanism for broadband frequency conversion into a coherent output frequency independently from the excitation frequencies.

Other potentially useful nonlinear behaviors exist outside the solitonic resonance domain, such as second

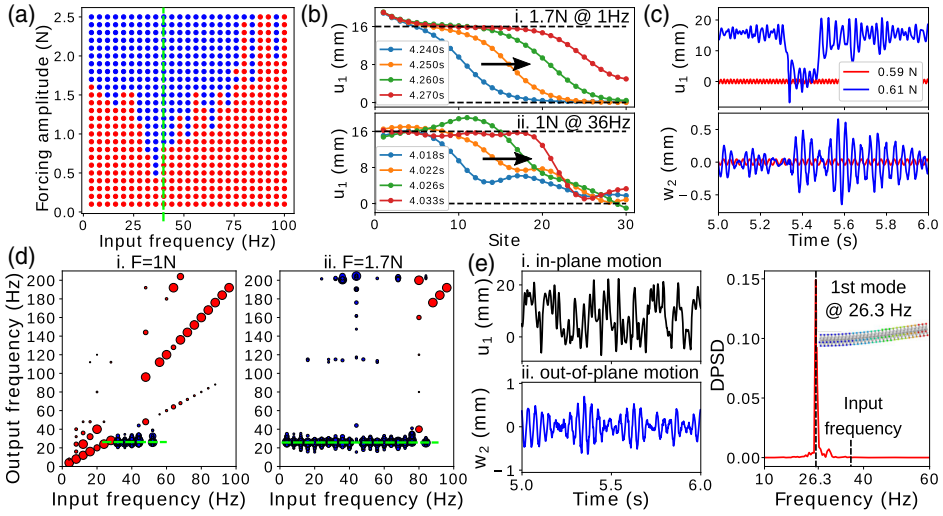

FIG. 4. (a) Response map in terms of input forcing amplitude and frequency, where blue dots indicate that transition waves are triggered. (b) In-plane displacements of the center masses in space configuration, showing transition wave propagation. (c) Response amplification when transition waves are triggered (in blue) compared to when they are not triggered (in red). (d) Output frequency diagrams for various input conditions, showing the output frequency spectrum for each input frequency. (e) Representative response of solitonic resonance, obtained for $F = 1$ N at 36 Hz.

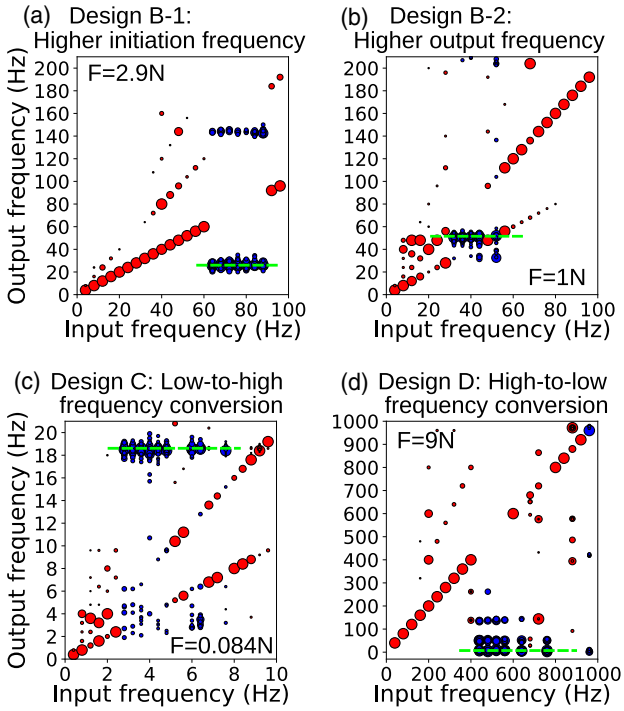

FIG. 5. Output frequency diagrams for various unit cell and external frame design combinations, demonstrating extreme tuning flexibility. (a) Design B-1 increases the initiation frequency of the solitonic resonance, and (b) design B-2 increases the output frequency. Output frequency diagrams for metabeam designs tuned to enable (c) low-to-high and (d) high-to-low frequency conversions, where the input and output frequencies are 1–2 orders of magnitude apart.

harmonic generation [between 12 and 20 Hz in Fig. 4(d)(i)] or frequency doubling (above 56 Hz) (Sec. 10 of Supplemental Material [27]). These will be addressed in detail in a separate study.

Tuning flexibility.—The simplicity and periodicity of the proposed metastructure allow the operating bandwidth to be easily tuned to suit a vast range of applications. The unit cell design dictates the central input frequency around which the solitonic resonance emerges, while the overall metastructure topology controls the corresponding output frequency. Quadrupling k_2 and k_3 doubles the in-plane unit cell mode, thus shifting up the input frequency inducing solitonic resonance [Fig. 5(a)]. On the other hand, quadrupling k_4–k_8 approximately doubles the macrostructure's original natural frequencies, moving the output frequency of solitonic resonance to a higher frequency range [Fig. 5(b)].

The metabeam can also be tuned to display remarkable energy exchanges between incommensurate frequency bands, which can be separated by several orders of magnitude. Two such examples are presented (see Supplemental Material [27] for the design parameters): one optimized to operate at 3–5 Hz range yielding ~18.63 Hz solitonic resonance [Fig. 5(c)] and the other at 400–560 Hz range yielding solitonic resonance below 10 Hz [Fig. 5(d)]. The tuning flexibility in the presented metastructures thus yields a blueprint for unprecedented dynamical manipulation from an intrinsically nonlinear interaction.

Conclusions.—We demonstrate nonlinear interactions involving solitary wave and vibration modes, resulting in extreme frequency conversion in generic bistable metastructures. Notably, the observed phenomenon referred to as solitonic resonance allows for a remarkably stable means to achieve input-independent frequency conversion, in which the output response is unaffected by wave dispersion. This behavior generalizes analogous fluxon-cavity mode resonance in superconducting electronics, providing an exemplary platform for frequency regulation and energy conversion applications across physical fields. The tuning flexibility of the presented metabeam also allows for extreme energy exchange between incommensurate frequencies separated by orders of magnitude. Importantly, the presented architecture provides a general model system for realizing unique properties in metamaterials at frequencies not dictated by the unit cell, opening up new avenues for attaining extreme dynamics.

The authors thank Professor C. Scalo for supporting the development of the in-house code. The authors are grateful for Dr. E. Arrieta Diaz's help in motivating this work beyond mechanics. We acknowledge the financial support from the National Science Foundation under Grant No. CMMI-1935137.

*aarrieta@purdue.edu

[1] M. Remoissenet, *Waves Called Solitons: Concepts and Experiments* (Springer, Berlin, 1996).
[2] D. N. Christodoulides and E. D. Eugenieva, Blocking and Routing Discrete Solitons in Two-Dimensional Networks of Nonlinear Waveguide Arrays, Phys. Rev. Lett. **87**, 233901 (2001).
[3] D. N. Christodoulides, F. Lederer, and Y. Silberberg, Discretizing light behaviour in linear and nonlinear waveguide lattices, Nature (London) **424**, 817 (2003).
[4] P. Marin-Palomo, J. N. Kemal, M. Karpov, A. Kordts, J. Pfeifle, M. H. P. Pfeiffer, P. Trocha, S. Wolf, V. Brasch, M. H. Anderson, R. Rosenberger, K. Vijayan, W. Freude, T. J. Kippenberg, and C. Koos, Microresonator-based solitons for massively parallel coherent optical communications, Nature (London) **546**, 274 (2017).
[5] W. Wustmann and K. D. Osborn, Reversible fluxon logic: Topological particles allow ballistic gates along one-dimensional paths, Phys. Rev. B **101**, 014516 (2020).
[6] M. C. Cassidy, A. Bruno, S. Rubbert, M. Irfan, J. Kammhuber, R. N. Schouten, A. R. Akhmerov, and L. P. Kouwenhoven, Demonstration of an ac Josephson junction laser, Science **355**, 939 (2017).
[7] A. Zareei, B. Deng, and K. Bertoldi, Harnessing transition waves to realize deployable structures, Proc. Natl. Acad. Sci. U.S.A. **117**, 4015 (2020).

[8] T. Singhal, E. Kim, T.-Y. Kim, and J. Yang, Weak bond detection in composites using highly nonlinear solitary waves, Smart Mater. Struct. **26**, 055011 (2017).
[9] B. Deng, L. Chen, D. Wei, V. Tournat, and K. Bertoldi, Pulse-driven robot: Motion via solitary waves, Sci. Adv. **6**, eaaz1166 (2020).
[10] A. Spadoni and C. Daraio, Generation and control of sound bullets with a nonlinear acoustic lens, Proc. Natl. Acad. Sci. U.S.A. **107**, 7230 (2010).
[11] A. M. Weiner, Cavity solitons come of age, Nat. Photonics **11**, 533 (2017).
[12] L. Ozyuzer, A. E. Koshelev, C. Kurter, N. Gopalsami, Q. Li, M. Tachiki, K. Kadowaki, T. Yamamoto, H. Minami, H. Yamaguchi, T. Tachiki, K. E. Gray, W. K. Kwok, and U. Welp, Emission of coherent THz radiation from superconductors, Science **318**, 1291 (2007).
[13] A. H. Nayfeh and D. T. Mook, *Nonlinear Oscillations* (Wiley, New York, 1995).
[14] P. Malatkar and A. H. Nayfeh, On the transfer of energy between widely spaced modes in structures, Nonlinear Dyn. **31**, 225 (2003).
[15] R. K. Narisetti, M. J. Leamy, and M. Ruzzene, A perturbation approach for predicting wave propagation in one-dimensional nonlinear periodic structures, J. Vib. Acoust. Trans. ASME **132**, 0310011 (2010).
[16] R. Khajehtourian and M. I. Hussein, Dispersion characteristics of a nonlinear elastic metamaterial, AIP Adv. **4**, 124308 (2014).
[17] R. Ganesh and S. Gonella, Nonlinear waves in lattice materials: Adaptively augmented directivity and functionality enhancement by modal mixing, J. Mech. Phys. Solids **99**, 272 (2017).
[18] R. Ganesh and S. Gonella, Experimental evidence of directivity-enhancing mechanisms in nonlinear lattices, Appl. Phys. Lett. **110**, 084101 (2017).
[19] X. Fang, J. Wen, D. Yu, G. Huang, and J. Yin, Wave propagation in a nonlinear acoustic metamaterial beam considering third harmonic generation, New J. Phys. **20**, 123028 (2018).
[20] M. Serra-Garcia, M. Molerón, and C. Daraio, Tunable, synchronized frequency down-conversion in magnetic lattices with defects, Phil. Trans. R. Soc. A **376**, 20170137 (2018).
[21] L. I. Manevich, A. V. Savin, V. V. Smirnov, and S. Volkov, Solitons in nondegenerate bistable systems, Usp. Fiz. Nauk **164**, 937 (1994).
[22] A. Cherkaev, E. Cherkaev, and L. Slepyan, Transition waves in bistable structures. I. Delocalization of damage, J. Mech. Phys. Solids **53**, 383 (2005).
[23] N. Nadkarni, C. Daraio, and D. M. Kochmann, Dynamics of periodic mechanical structures containing bistable elastic elements: From elastic to solitary wave propagation, Phys. Rev. E **90**, 023204 (2014).
[24] N. Nadkarni, A. F. Arrieta, C. Chong, D. M. Kochmann, and C. Daraio, Unidirectional Transition Waves in Bistable Lattices, Phys. Rev. Lett. **116**, 244501 (2016).
[25] J. R. Raney, N. Nadkarni, C. Daraio, D. M. Kochmann, J. A. Lewis, and K. Bertoldi, Stable propagation of mechanical signals in soft media using stored elastic energy, Proc. Natl. Acad. Sci. U.S.A. **113**, 9722 (2016).
[26] M. Hwang and A. F. Arrieta, Input-independent energy harvesting in bistable lattices from transition waves, Sci. Rep. **8**, 3630 (2018).
[27] See Supplemental Material at http://link.aps.org/supplemental/10.1103/PhysRevLett.126.073902 for additional details about the metabeam designs, experimental method, theoretical investigation, and numerical results, which include Ref. [28,29]. Movie S1 illustrates the coupling between the in-plane and out-of-plane motions. Movie S2 and S3 show the experimental and numerical demonstrations of solitonic resonance.
[28] H. M. Hilber, T. J. R. Hughes, and R. L. Taylor, Improved numerical dissipation for time integration algorithms in structural dynamics, Earthquake Eng. Struct. Dyn. **5**, 283 (1977).
[29] M. Hwang and A. F. Arrieta, Energy harvesting characteristics in metamaterials based on bistable lattices, in *Active and Passive Smart Structures and Integrated Systems XIII*, edited by A. Erturk (SPIE, Bellingham, WA, 2019), p. 13.
[30] J. Thompson and H. Stewart, *Nonlinear Dynamics and Chaos* (Wiley, New York, 2002).
[31] T. Dauxois and M. Peyrard, *Physics of Solitons* (Cambridge University Press, Cambridge, England, 2006).
[32] H. Kulah and K. Najafi, Energy scavenging from low-frequency vibrations by using frequency up-conversion for wireless sensor spplications, IEEE Sens. J. **8**, 261 (2008).
[33] Both excitation types are very common in engineering applications. The force input is relevant for either rotating unbalanced mass or noncontacting sources, and the displacement input is relevant for a contacting excitation source, especially when its inertia is large such that the reaction force from the structure hardly affects the motion of the source.
[34] The next dominant branch appears at ~24.5 Hz, which is the second macroscopic structural mode.
[35] L. N. Virgin, *Introduction to Experimental Nonlinear Dynamics* (Cambridge University Press, Cambridge, England, 2000).

SUPPLEMENTAL MATERAL for
Extreme Frequency Conversion from Soliton Resonant Interactions

M. Hwang and A. F. Arrieta

February 10, 2021

1 Experimental method

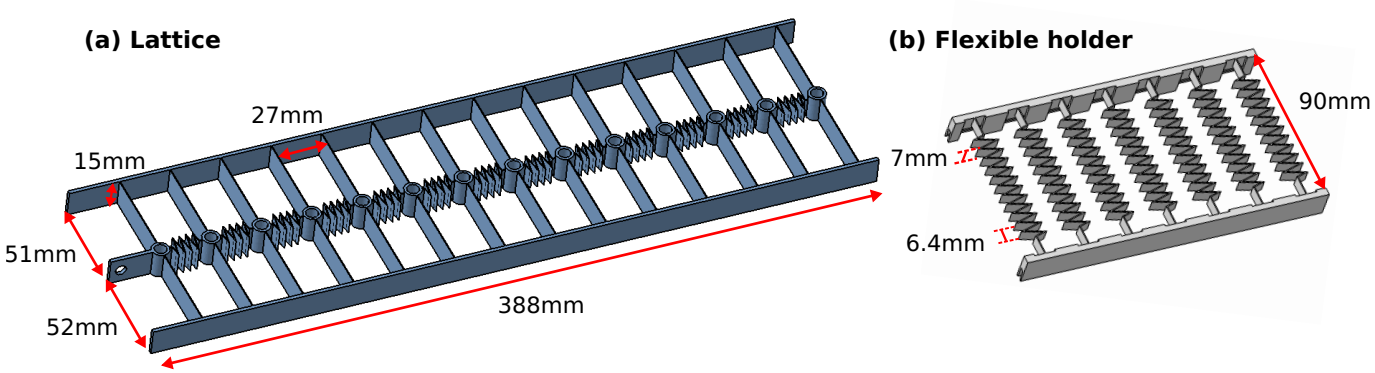

FIG. S1: CAD models for (a) the lattice and (b) the flexible holder with key geometric dimensions shown.

The experimental demonstrator is prepared by assembling multiple parts printed with a fused-deposition-modeling 3D printer (Ultimaker 3 Extended). First, a lattice structure [the black component in Fig. 1(a) in the manuscript and Fig. S1(a)] is 3D-printed in black PLA material, where the ribs are interconnected by spring-like features.[1] The lattice axis (along the intersite springs) is slightly offset from the centerline of the structure so as to amplify the flexural motion. Next, a set of four flexible holders [the white component in Fig. 1(a) and Fig. S1(b)] are printed in white PLA and fitted with the flanges of the lattice structure. Upon assemblage, the holders precompress the lattice to allow two different stable states [Figs. 1(a)(i) and 1(a)(ii)] and provide flexibility in the transverse direction. The cylindrical hole at the center of each unit cell is filled with ∼2.6 g of solder to increase the inertia of unit cells. The fixed-free boundary condition is realized by clamping the flanges at one end of the assembled structure to the rigid test rig and leaving the other end unconstrained [Fig. 1(a)(iii)].

The metabeam is excited by APS 113 long-stroke electrodynamic shaker powered by APS 125 power amplifier. An open-loop control system is designed in Simulink, and a sinusoidal input signal is sent through dSpace data acquisition system (DS1104) to control the shaker. The amplitude of the input signal is controlled by manually changing the amplifier gain; the gain is increased until noticeable periodic motions start for the small-amplitude responses and until the transition waves are generated in the metabeam for the large-amplitude responses. Due to the shaker's limited capability, only approximate displacement-controlled tests are performed. Although the reaction force from the demonstrator affects the shaker force, its effect is minimal due to the heavy armature weight (2.5 kg), which is cross-checked by measuring the input displacements with a laser displacement sensor (Keyence LK-H157) pointing at the flat surface of the shaker head. The measured input displacements are almost sinusoidal with small contributions from the higher harmonics, which becomes vanishingly small as the input frequency increases further due to the increased inertial effect of the moving parts of the shaker.[2] The output responses are measured by another laser sensor, pointing to one of the beam surfaces near the free end, as shown in Fig. 1(a)(iii).

[1] The maximum build plate size of Ultimaker 3 Extended is 215 mm, and so the lattice structure is printed in two pieces and glued together.

[2] Refer to the following section for the measured displacements

2 Selected experimental results

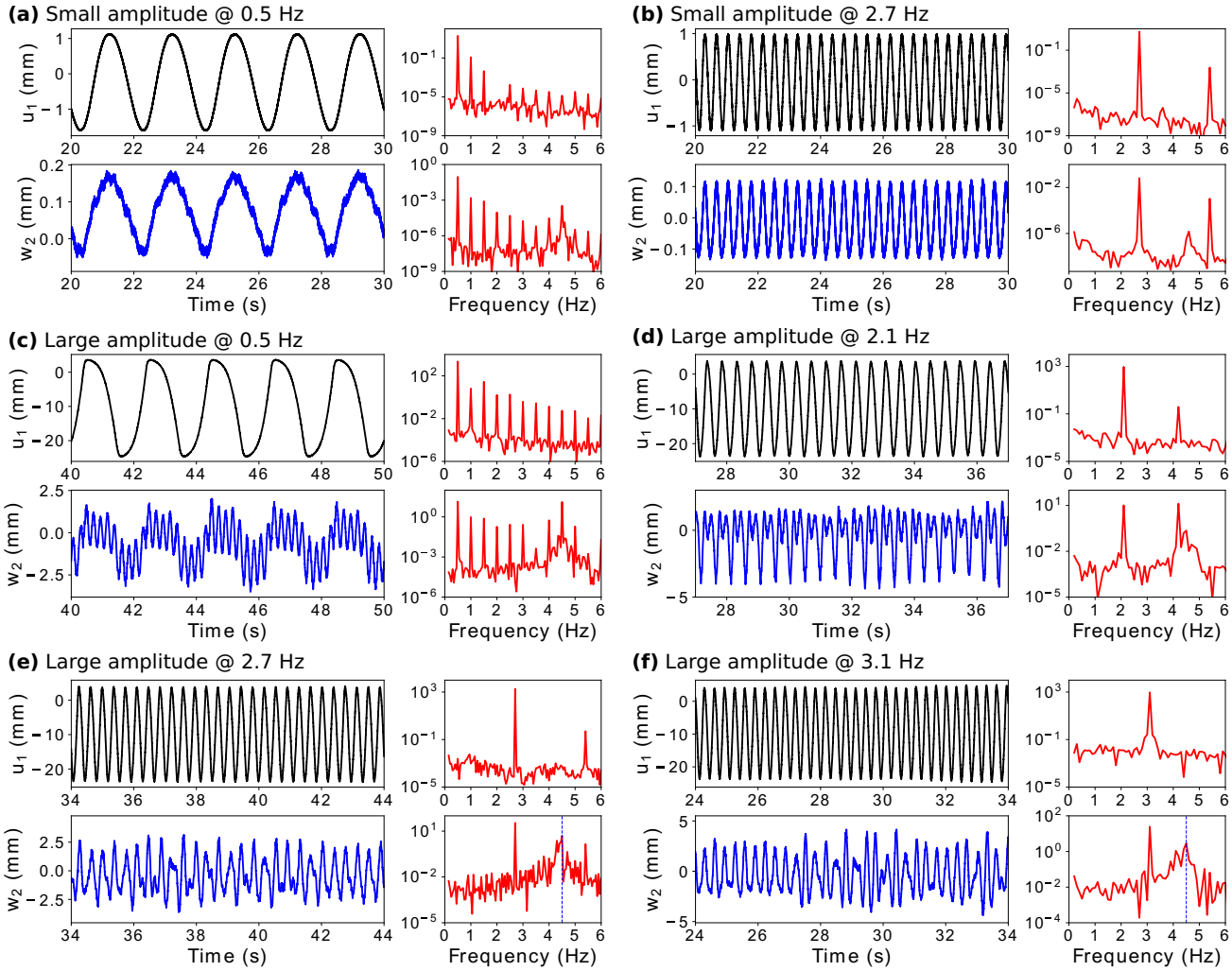

FIG. S2: Selected experimental results. (a,b) Metabeam responses for 0.5 Hz and 2.7 Hz under small-amplitude displacement inputs yielding direct correspondence between the input and the dominant output frequencies. (c,d) Metabeam responses for 0.5 Hz and 2.1 Hz under large-amplitude displacement inputs yielding superharmonic resonances of the input frequencies. (e,f) Metabeam responses for 2.7 Hz and 3.1 Hz, showing solitonic resonance (blue dashed line), the frequency content of which is incommensurate with the input frequency.

Some of the measured time responses w_2's and the associated DPSD's are presented in Fig. S2. The applied displacements u_1's are not purely sinusoidal but contain the harmonics of the input frequency due to the reaction force from the metabeam sample. However, these harmonic contributions are minimal compared to the input frequency, especially for higher input frequencies. Under small-amplitude input displacements, the input frequency contributions are directly reflected in the DPSD, exhibiting typical linear and weakly nonlinear behaviors [Figs. S2(a) and S2(b)]. For large-amplitude input displacements that trigger transition waves, the contributions from the harmonics of the input frequency are emphasized. For input frequencies whose integer multiples are close to the natural frequency of the metabeam (∼4.62 Hz), superharmonic resonances occur as can be identified by the spikes at the corresponding harmonics of the input frequencies [Figs. S2(c) and S2(d)]. However, for input frequencies whose harmonics are not close to the natural frequency of the metabeam, a totally unrelated frequency component appears, which is due to the transient effect from the generated transition waves [dashed line in Figs. S2(e) and S2(f)]. This constitutes incommensurate frequency generation, a signature of the solitonic resonance phenomenon.

3 Natural frequencies of the experimental demonstrator

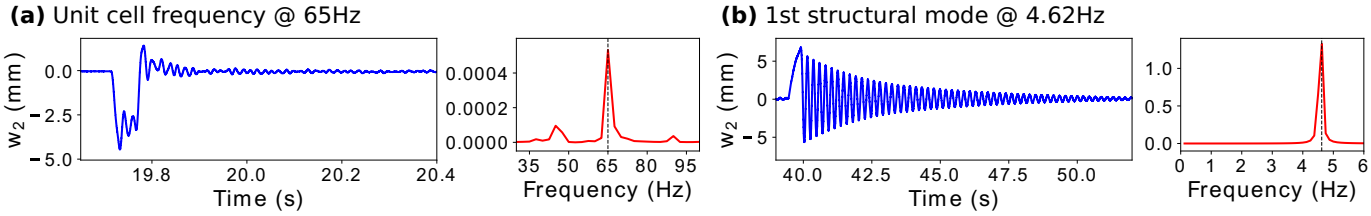

FIG. S3: Measured free vibration responses and the corresponding power spectral densities for (a) the unit cell and (b) the macroscopic structure under impulsive inputs.

The natural frequency of the unit cell is obtained by gently hammering the first element in the in-plane direction and measuring its free response. This bistable element is disconnected from the neighboring unit cell to avoid measuring the natural frequencies of the coupled system modes. To find the dominant frequency, we analyze the response signal between 20 and 20.4 s, where the vibration amplitudes are small enough to minimize the shift from nonlinear effects. The dominant mode occurs at ∼65 Hz [Fig. S3(a)]. For the structural mode, a small initial displacement is applied at the free end, and then the resulting free response is measured. The signal is analyzed between 44 and 52 s to obtain the frequency content, and the natural frequency is measured to be ∼4.62 Hz [Fig. S3(b)].

4 Beam subjected to a moving particle

The fundamental dynamics in soliton-metastructure interactions can be described by a beam subjected to in-plane moving particles. The motion of a single particle traveling along the beam's length can be mathematically represented as a traveling impulse $p(x,t) = P\delta\big(x - c(t - mT)\big)$ for $mT < t < mT + \frac{L}{c}$, where P, c, L, δ, m, and T are the forcing amplitude, the particle speed, the beam's length, Dirac-Delta function, an integer from 0 to the number M of particles sent in series, and the period of excitation, respectively. The period of the excitation in this context is not the one for the simple harmonic motion but indicates the time interval between two traveling particles. Assuming an Euler-Bernoulli beam, we can write coupled equations for the longitudinal displacement $u(x,t)$ and transverse displacement $v(x,t)$ in the following general form:

$$\begin{aligned} EA\frac{\partial^2 u(x,t)}{\partial x^2} - G\frac{\partial^3 v(x,t)}{\partial x^3} - \rho A\frac{\partial^2 u(x,t)}{\partial t^2} &= p(x,t). \\ EI\frac{\partial^4 v(x,t)}{\partial x^4} - G\frac{\partial^3 u(x,t)}{\partial x^3} + \rho A\frac{\partial^2 v(x,t)}{\partial t^2} &= \frac{\partial p(x,t)}{\partial x}, \end{aligned} \tag{S.1}$$

where the axial stiffness EA, bending stiffness EI, coupling stiffness G, density ρ, and cross-sectional area A are constant. Aligning the x-coordinate direction along the neutral axis (centroidal axis), the equations of motion can be decoupled. The uncoupled equation for $v(x,t)$ is:

$$EI\frac{\partial^4 v(x,t)}{\partial x^4} + \rho A\frac{\partial^2 v(x,t)}{\partial t^2} = e\frac{\partial p(x,t)}{\partial x}, \tag{S.2}$$

where e is an eccentricity from the centroid, and the variables and the parameters are redefined according to the changed coordinate x. This resulting e couples the longitudinal and transverse motions, thus justifying the introduction of the offset between the main axis of the bistable lattice and the centerline of the metabeam in both the experimental and numerical models.

Eq. (S.2) can be solved by a modal expansion $v(x,t) = \sum_{n=1}^{\infty} q_n(t)\phi_n(x)$, where $q_n(t)$'s are the generalized Fourier coefficients corresponding to the normal modes $\phi_n(x)$'s. The normal modes can be obtained by solving the associated homogeneous problem

$$\phi''''(x) - \beta_n^4\phi(x) = 0, \tag{S.3}$$

where $\beta_n^4 = \frac{\omega_n^2}{a^2}$, $\omega_n = 2\pi f_n$, $a^2 = \frac{EI}{\rho A}$, and the prime represents the derivative with respect to x. One way to represent the normal modes of a fixed-free beam is

$$\phi_n(x) = (\cos\beta_n x - \cosh\beta_n x) + \zeta_n(\sin\beta_n x - \sinh\beta_n x), \tag{S.4}$$

where $\zeta_n = \frac{\sin\beta_n L - \sinh\beta_n L}{\cos\beta_n L + \cosh\beta_n L}$, and the eigenvalue β_n can be obtained from the roots of the characteristic equation $\cos\beta_n L\cosh\beta_n L = 1$.

Substituting $v(x,t)$ into Eq. (S.2) and using Eq. (S.3),

$$\sum_{n=1}^{\infty}[\ddot{q}_n(t)+a^2\beta_n^4 q_n(t)]\phi_n(x)=b\delta'(x-ct), \tag{S.5}$$

where $b=\frac{eP}{\rho A}$. Using the orthogonality of $\phi_n(x)$'s, we obtain an ordinary differential equation for $q_n(t)$:

$$\ddot{q}_n(t)+a^2\beta_n^4 q_n(t)=\frac{\int b\delta'(x-ct)\phi_n(x)dx}{W_n}=\frac{-b\phi_n(ct)}{W_n}. \tag{S.6}$$

where $W_n=\int\phi_n^2(x)dx$. Assuming zero initial conditions [$v(0)=0$, $\dot{v}(0)=0$], the solution for $q_n(t)$ can be obtained from the method of variation of parameters:

$$q_n(t)=\begin{cases}-\frac{b}{\omega_n W_n}\sum_{i=0}^{m}\int_{iT}^{t}\phi_n'\big(c(\tau-iT)\big)\sin\omega_n(t-\tau)d\tau & \text{for } mT<t\le mT+\frac{L}{c}\\ -\frac{b}{\omega_n W_n}\sum_{i=0}^{m}\int_{iT}^{iT+\frac{L}{c}}\phi_n'\big(c(\tau-iT)\big)\sin\omega_n(t-\tau)d\tau & \text{for } mT+\frac{L}{c}<t<(m+1)T,\end{cases} \tag{S.7}$$

yielding solutions of the form:

$$q_n(t)=\begin{cases}a_{nm}\sin(\omega_n t+\theta_{nm})+b_{nm}\phi_n\big(c(t-mT)\big) & \text{for } mT<t\le mT+\frac{L}{c}\\ c_{nm}\sin(\omega_n t+\tilde{\theta}_{nm}) & \text{for } mT+\frac{L}{c}<t\le(m+1)T,\end{cases}$$

where a_{nm}, b_{nm}, and c_{nm} are the constants determined by the system parameters, and θ_{nm} and $\tilde{\theta}_{nm}$ are the phase constants.

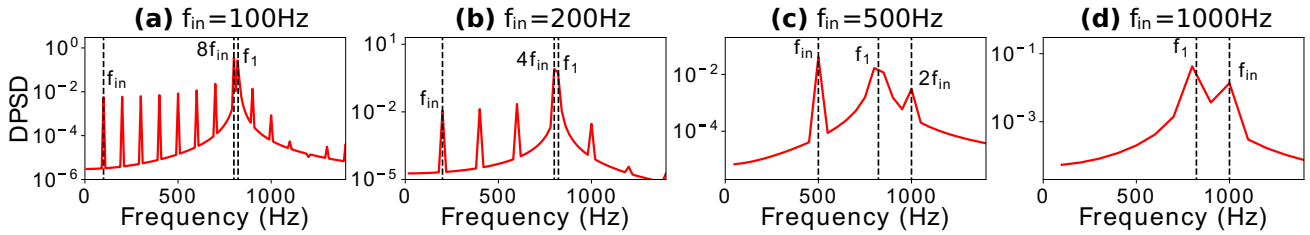

FIG. S4: Power spectral densities of the approximated tip displacements of a fixed-free metabeam under (a) $f_{\text{in}}=100$ Hz, (b) $f_{\text{in}}=200$ Hz, (c) $f_{\text{in}}=500$ Hz, and (d) $f_{\text{in}}=1000$ Hz.

We obtain example responses of the fixed-free beam with a 5-term approximation: $v(x,t)=\sum_{n=1}^{5}q_n(t)\phi_n(x)$. The following parameters are used for the examples: $EI=70{,}000$ MPa, $\rho=2.7\times10^{-9}$ tonne, $w=10$ mm, $h=10$ mm, $L=100$ mm, $e=3$ mm, $P=10{,}000$ N/mm, and $c=100{,}000$ mm/s. Twenty-two particles (traveling impulses) are sent in series, and the frequency responses are obtained between $12T$ and $22T$ s. Figure S4 shows the DPSD's of the tip displacements under various input frequencies $f_{\text{in}}=1/T$. For the input frequencies f_{in}'s whose harmonics are close to the fundamental mode f_1 (= 823 Hz) of the metabeam, the most dominant response occurs at these harmonics [Figs. S4(a) and S4(b)]. Even for the input frequencies which do not have immediate integer relationships close to the fundamental mode, the frequency contribution corresponding to the fundamental frequency still remains [Figs. S4(c) and S4(d)].[3] These results are in agreement with the experimentally observed behaviors.

[3]The slight mismatch between the frequency peak and f_1 is due to the frequency discretization size. For example, the discretization size is 100 Hz in Fig. 4(d) so that the peak appears at 800 Hz, the closest bin to f_1 (823 Hz).

5 Metabeam description and design parameters

A rectangular building block forming the external frame of the metabeam is composed of the linear springs with constants k_4, k_5, and k_6 connecting the point masses m_2 and m_3 at the top and bottom vertices, respectively, and two diagonal springs with constants k_7 and k_8 providing static stability to the frame [refer to Fig. 3(a) in the manuscript]. Stemming from the top and bottom masses are linear springs with constants k_2 and k_3 joining the center mass m_1 at an angle, forming a bistable mechanism. For all examples in this study, the value of k_2 is chosen such that the spring forces are balanced in the out-of-plane direction[4] under small perturbations along the main lattice axis so that the unit cell mass does not incur an excessive transverse fluctuation while undergoing interwell oscillations. The center masses of the neighboring bistable elements are then connected to one another by the linear intersite springs with stiffness k_1. For the numerical simulations in this study, the mass proportional damping with a coefficient γ is applied to suppress unwanted transient dynamics. The governing equations of motion can be found in Sec. 11 of this Supplemental Material.

Table S1 lists the sets of design parameters for all the metabeam designs appearing in this study. Design A is a qualitatively similar design to the experimental metabeam. For Design A, the design parameters are adjusted to yield closely approximate values for the size of the metastructure (14 unit cells 27 mm apart), the natural frequency of the unit cell (65 Hz), and that of the macrostructure (4.62Hz) to those of the experimental demonstrator. Design A-1 and Design A-2 are the variations of Design A, where only the mass proportional damping coefficient values are increased and decreased to observe the effect of system damping on the output frequency spectrum under low-frequency excitations. Design B is the baseline design for the metabeam under force excitation. The parameters for Design B are selected such that the metabeam operates in the 0-100 Hz range. We use $k_2 = 1.076$ N/mm and $k_3 = 0.6$ N/mm for the bistable microstructure, yielding the unit cell mode at 39.7 Hz. $k_1 = 1.241$ N/mm is chosen to minimize the discreteness effects of the lattice.[5] For design simplicity, the baseline values for k_4, k_5, k_6, k_7, and k_8 are selected to have the same stiffness, 1,500 N/mm, yielding the fundamental macroscopic mode at 26.3 Hz. The coefficient γ is chosen to be 9.91 s^{-1} so that the decay rate corresponds to the damping ratio $\zeta = 0.03$ with respect to the fundamental structural mode. Design B-1 shifts the operating frequency band (input frequencies initiating the solitonic resonance) to a higher frequency region from that of Design B. This is achieved by stiffening the springs forming the bistable elements (springs with constants k_2 and k_3) from the baseline design since the transition wave generation, which leads to the solitonic resonance, is governed by the resonant excitation of the bistable unit cell in the in-plane direction. Design B-2 shifts the output frequency of the solitonic resonance to a higher frequency region. The springs forming the external frames (springs with constants k_4, k_5, k_6, k_7, and k_8) govern the natural frequencies of the macrostructural modes and are thus stiffened to increase the output frequency. Design C and D demonstrate the extreme tunability that allows frequency conversion between frequencies several orders of magnitude apart. The internal bistable microstructure of Design C (Design D) is tuned to have a very low (high) natural frequency to achieve an extreme low-to-high (high-to-low) frequency conversion.

	k_1	k_2	k_3	k_4, k_5	k_6	k_7, k_8	m_1	m_2, m_3	L_1	L_2	L_3	R	γ	N
Design A	4	13.9	13.3	6.35	20	20	5	5	27	46	44	8	3.19	14
Design A-1	4	13.9	13.3	6.35	20	20	5	5	27	46	44	8	5.81	14
Design A-2	4	13.9	13.3	6.35	20	20	5	5	27	46	44	8	0.319	14
Design B	1.241	1.076	0.6	1,500	1,500	1,500	2	1	20	40	20	8	9.91	30
Design B-1	4.96	4.30	2.4	1,500	1,500	1,500	2	1	20	40	20	8	9.91	30
Design B-2	1.241	1.076	0.6	6,000	6,000	6,000	2	1	20	40	20	8	9.91	30
Design C	0.1	0.242	0.2	1600	100	800	20	10	25	55	45	8	0.708	20
Design D	96.3	100.2	70	800	800	800	1	1	5	6	4	1.2	31.3	40

TAB. S1: Summary of the parameters for each metabeam design. The units of the stiffness k_i's, mass m_i's, distance L_i's and R, and mass proportional damping coefficient γ are N/mm, g, mm, and s^{-1}, respectively. N is the number of unit cells forming the metabeam.

[4]The metabeam is defined in a 2D space. In this study, the in-plane direction is the direction along the bistable lattice, and the out-of-plane (or transverse) direction is the direction perpendicular to the in-plane direction.

[5]The ratio between k_1 and the effective in-plane stiffness $k_{\text{eff}} = \left(\frac{k_2}{L_2^2+R^2} + \frac{k_3}{L_3^2+R^2}\right) R^2$ of the bistable unit cell affects the lattice discreteness [1, 2] and is ∼10 for the selected stiffness values.

6 Metabeams under a different boundary condition

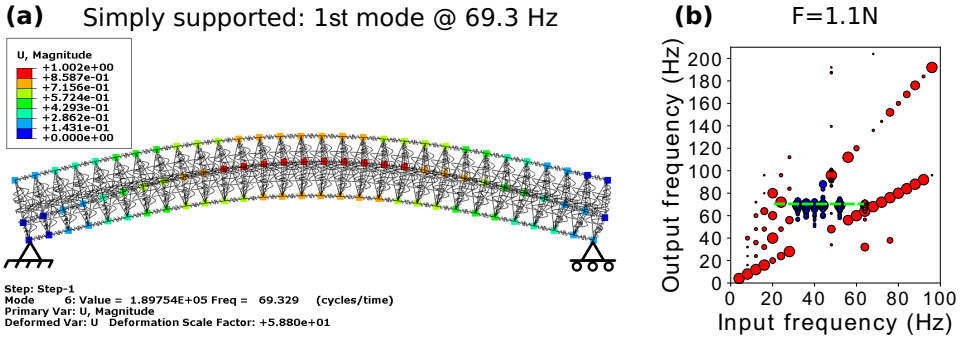

FIG. S5: (a) Fundamental structural mode of Design B under the simply-supported boundary condition. (b) The corresponding output frequency diagram under $F = 1.1$ N, exhibiting solitonic resonance at the fundamental mode.

The input-independent frequency conversion into a single dominant frequency (solitonic resonance) is a robust phenomenon not tied to a specific boundary condition. The simply-supported boundary condition is simulated by fixing the leftmost bottom node and constraining the out-of-plane motion of the rightmost bottom node. All design parameters are kept the same as those of Design B, and the changed boundary condition shifts the first structural mode to 69.3 Hz [Fig. S5(a)]. For a sufficiently large input force that can trigger transition waves, the same characteristic behavior (input-independent output frequency at the structural mode) remains for the domain where transition waves are generated as shown in Fig. S5(b).

7 Damping effect in the low input frequency domain

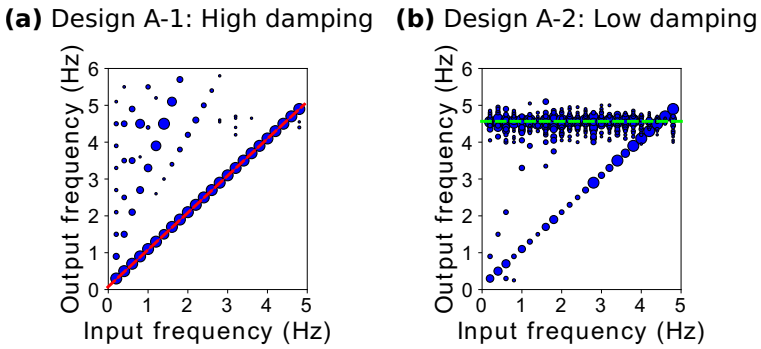

FIG. S6: Output frequency diagrams for the qualitatively similar numerical design under (a) high and (b) low system damping.

Since the output frequency branch near the macroscopic structural mode arises due to the repeated transient effects from the traveling transition waves, the degree of the system damping greatly affects which solution branch dominates the response. For a large proportional damping coefficient $\gamma = 5.81$ s^{-1} compared to that of the qualitatively similar design in the manuscript (Design A), the solitonic resonance branch begins to disappear [Fig. S6(a)]. On the other hand, for very low proportional damping coefficient $\gamma = 0.319$ s^{-1}, the solitonic resonance branch is accentuated, becoming qualitatively closer to a complete input-independent transformation [Fig. S6(b)].

8 Amplification by solitonic resonance

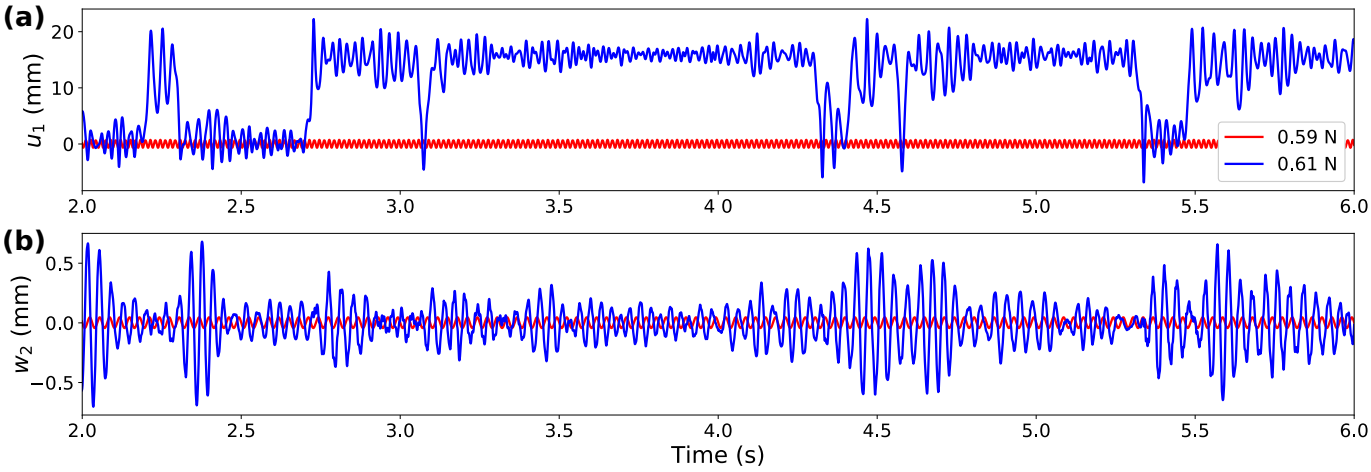

FIG. S7: (a) In-plane displacement of the center node and (b) the out-of-plane displacement of the top node at the rightmost unit cell under 32 Hz inputs near the critical forcing amplitude yielding solitonic resonance. There is drastic amplification of the motion when solitonic resonance occurs (at 0.61 N plotted in blue), compared to the case solitonic resonance is not triggered (at 0.59 N plotted in red).

Since solitonic resonance relies on a series of transition waves, which appear as high-orbit interwell oscillations for each element of the underlying bistable lattice, a larger-amplitude macroscopic behavior is expected, compared to the case where transition waves are not triggered. At 32 Hz input frequency, for example, the critical forcing amplitude that enables solitonic resonance is about 0.6 N. The responses under forcing amplitudes just before and after solitonic resonance are plotted in Fig. S7. Figure S7(a) shows the in-plane displacements of the center node at the rightmost unit cell. The jumps between the two equilibrium points (0 mm and 16 mm) indicate that transition waves are triggered under 0.61 N input (plotted in blue), as opposed to small fluctuations about one of the equilibrium points under 0.59 N input (plotted in red).[6] Figure S7(b) shows the corresponding out-of-plane displacements of the top node at the rightmost unit cell, and the maximum amplitude is ∼14 times larger when solitonic resonance occurs than the case it does not. The increase in the forcing amplitude is only ∼3.4%, yet the output displacements associated with solitonic resonance is much larger. In other words, the excitation of solitonic resonance shows the hallmark signal amplification effect in resonant responses.

9 Solitonic resonance from noisy sources

Solitonic resonance can also be excited by inputs with broadband spectra. To demonstrate this, we generate noisy signals by combining multiple sinusoidal inputs whose frequencies $\tilde{f}_i$'s are incommensurate with one another to excite the metabeams. The frequency components are obtained from a power-law relationship $\tilde{f}_i = \frac{1}{3}\pi i^{1.42}$ between 0–200 Hz. The sinusoids are prepared with alternating phases to avoid an initial abrupt force peak; as time progresses, the combined signals become more randomly dispersed due to the incommensurate frequency relationship, thereby resulting in a noisy excitation. The final form of the noise is $n(t) = \sum_i A_i(-1)^{i+1} \sin 2\pi \tilde{f}_i t$, where A_i is the amplitude of each sinusoid, which is set equal to one another to simulate approximately randomly distributed excitation spectrum. In the limit, this tends to white noise. The mass proportional damping coefficient is reduced to 3.30 s^{-1} from the baseline design to facilitate state transition, and the simulation is run for a sufficiently long period (80 s) to capture the random effects from the noisy inputs. The power spectral densities of the input force (FPSD) and the output displacement (DPSD) are obtained from the response between 70 and 80 s.

The intensity of the noise is increased until an in-plane direction state transition is triggered at the excitation site; the first occurrence of the state transition is observed at $A = 0.066$ N [see Fig. S8(a)]. However, the rate of the occurrence of the transition waves is intermittent and random, which cannot be used as a reliable source of coherent output frequency generation. We add a small sinusoidal input (0.11 N at 35 Hz that is near the resonant frequency of the unit cell) on top of the noise to promote more frequent interwell oscillations necessary for generating solitonic

[6]The in-plane displacement is larger near the excitation site (∼4 mm); however, its wave amplitude does not propagate to the opposite end of the structure due to the system dissipation. Solitonic resonance does not exhibit such dissipation in wave amplitudes throughout the bistable lattice since unattenuated propagation is a hallmark of transition waves.

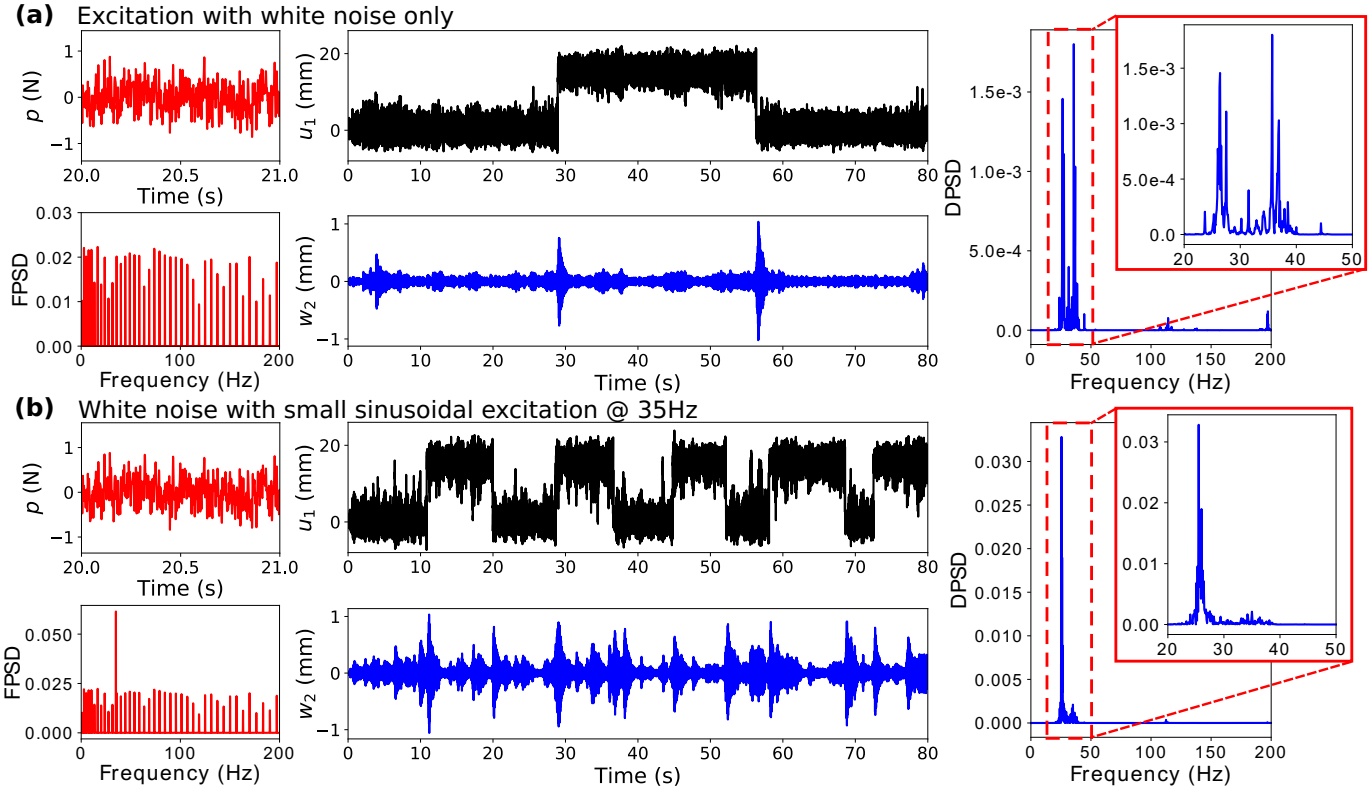

FIG. S8: Responses of the metabeam under (a) a white noise only and (b) a combined input with both white noise and small sinusoidal excitation. p is the input force, u_1 is the in-plane displacement obtained at the excitation site, and w_2 is the out-of-plane displacement obtained at the top node of the rightmost unit cell.

resonance. The effect of this additional input component is small as the required forcing amplitude to trigger transition waves from a purely sinusoidal input at 35 Hz is $\sim$0.55 N. The output responses under this combined excitation are plotted in Fig. S8(b). The in-plane displacement u_1 at the excitation site shows that interwell oscillations occur more often than the case under noise only. Specifically, the resulting out-of-plane displacement w_2 of the top node at the rightmost unit cell and its DPSD display a single dominant output frequency near the macrostructural mode. In other words, a small fraction of the input energy otherwise required for a perfect system is enough to yield solitonic resonance under the presence of noise. Thus, solitonic resonance will be enhanced in realistic conditions, which inevitably are subjected to noisy perturbations. Importantly, this result implies that even noisy sources (e.g., colored inputs) can be transformed into a single coherent mode through the strongly nonlinear interaction with the metabeam.

10 Characteristic time responses

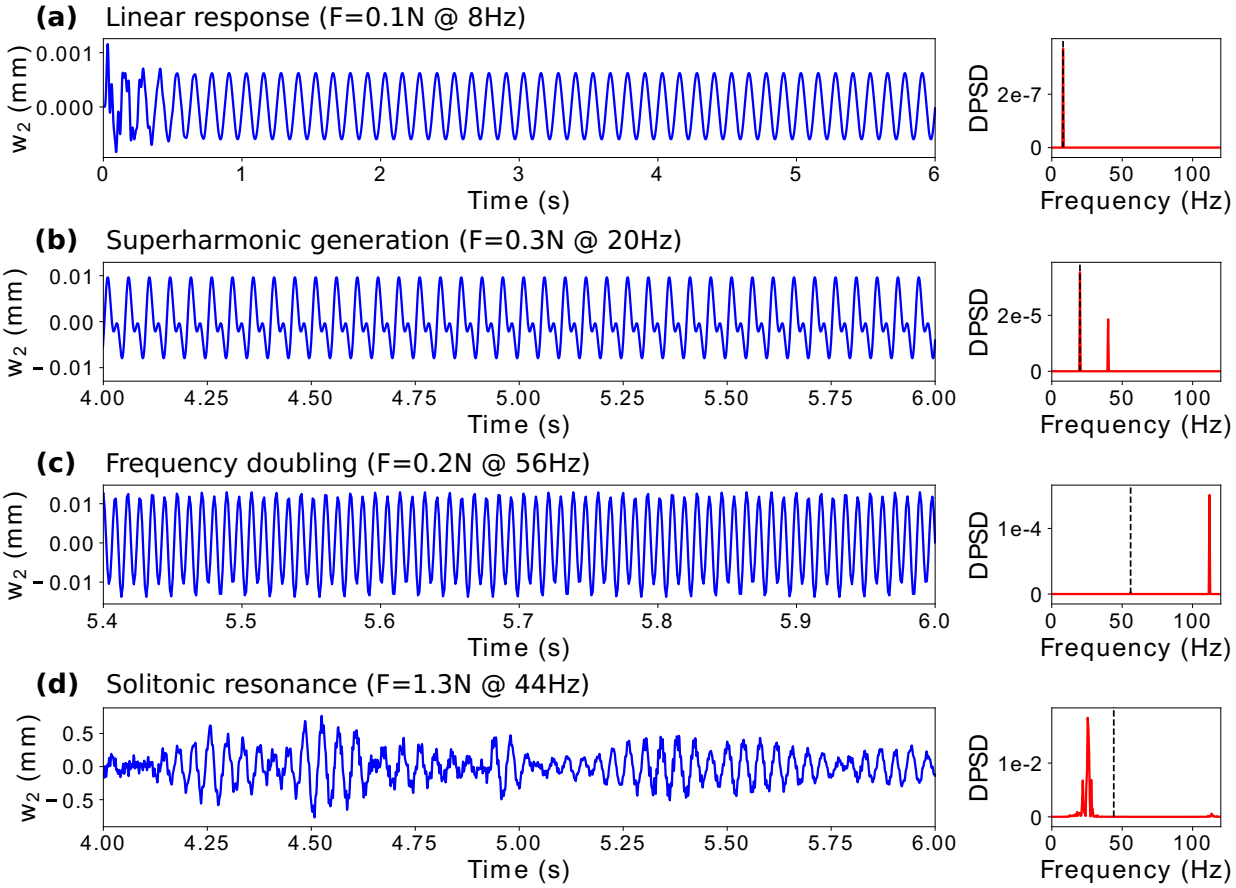

FIG. S9: Four characteristic time responses of the metabeam and their power spectral densities: (a) linear response whose output frequency corresponds to the input frequency, (b) generation of superharmonic contribution to the input frequency, (c) frequency doubling, and (d) solitonic resonance. The input frequencies are indicated by the black dashed lines.

Four characteristic time responses that can be observed in the studied metabeam are plotted in Fig. S9. For a very small force input, the output frequency directly corresponds to the input frequency [Fig. S9(a)]. When operated in a weakly nonlinear regime, the second harmonic frequency begins to contribute to the output response. Depending on where the output frequencies fall on the dispersion relation, both of the frequency contributions may coexist [Fig. S9(b)], or either of the contributions may cut off, leading to linear response or frequency doubling [Fig. S9(c)].[7] Finally, solitonic resonance occurs when transition waves are triggered within the metabeam [Fig. S9(d)]; the dominant frequency is totally unrelated to the input frequency.

[7] Their complete characterization will be addressed in a separate study

11 Governing equations

Each unit cell of the metabeam has 6 degrees of freedom, and the equations of motion can be derived from the Euler-Lagrangian method. The Lagrangian $\mathcal{L} = \mathcal{T} - \mathcal{V}$ can be readily written as

$$\begin{aligned}\mathcal{T} &= \sum_{n-1}^{N}\left[\frac{1}{2}m_1(\dot{u}_{1,n}^2+\dot{w}_{1,n}^2)+\frac{1}{2}m_2(\dot{u}_{2,n}^2+\dot{w}_{2,n}^2)+\frac{1}{2}m_3(\dot{u}_{3,n}^2+\dot{w}_{3,n}^2)\right]\\ \mathcal{V} &= \sum_{n=1}^{N}\left[\frac{1}{2}k_2\Delta_2^2+\frac{1}{2}k_3\Delta_3^2+\frac{1}{2}k_6\Delta_6^2\right]+\sum_{n=1}^{N-1}\left[\frac{1}{2}k_1\Delta_1^2+\frac{1}{2}k_4\Delta_4^2+\frac{1}{2}k_5\Delta_5^2+\frac{1}{2}k_7\Delta_7^2+\frac{1}{2}k_8\Delta_8^2\right],\end{aligned} \tag{S.8}$$

where $\mathcal{T}$ and $\mathcal{V}$ are the system's total kinetic and potential energies, N is the number of unit cells, and $u_{m,n}$ and $w_{m,n}$ are the in-plane and out-of-plane displacements of the mth mass of the nth unit cell, respectively. The corresponding spring deflection Δ_i for each spring with stiffness k_i is given as:

$$\begin{aligned}\Delta_1 &= \sqrt{(L_1+u_{1,n+1}-u_{1,n})^2+(w_{1,n+1}-w_{1,n})^2}-L_1\\ \Delta_2 &= \sqrt{(R+u_{2,n}-u_{1,n})^2+(L_2+w_{2,n}-w_{1,n})^2}-\sqrt{R^2+L_2^2}\\ \Delta_3 &= \sqrt{(R+u_{3,n}-u_{1,n})^2+(L_3+w_{1,n}-w_{3,n})^2}-\sqrt{R^2+L_3^2}\\ \Delta_4 &= \sqrt{(L_1+u_{2,n+1}-u_{2,n})^2+(w_{2,n+1}-w_{2,n})^2}-L_1\\ \Delta_5 &= \sqrt{(L_1+u_{3,n+1}-u_{3,n})^2+(w_{3,n+1}-w_{3,n})^2}-L_1\\ \Delta_6 &= \sqrt{(u_{2,n}-u_{3,n})^2+(L_2+L_3+w_{2,n}-w_{3,n})^2}-(L_2+L_3)\\ \Delta_7 &= \sqrt{(L_1+u_{2,n+1}-u_{3,n})^2+(L_2+L_3+w_{2,n+1}-w_{3,n})^2}-\sqrt{L_1^2+(L_2+L_3)^2}\\ \Delta_8 &= \sqrt{(L_1+u_{3,n+1}-u_{2,n})^2+(L_2+L_3+w_{2,n}-w_{3,n+1})^2}-\sqrt{L_1^2+(L_2+L_3)^2}.\end{aligned} \tag{S.9}$$

Additionally, small dissipation is applied in the form of a mass proportional damping with a coefficient γ to suppress any unwanted transient effect. The full expressions of the governing equations for the nth unit cell are shown at the end of this section.

The obtained set of discrete equations is highly coupled and nonlinear involving several radical expressions. There exists no exact solution, and thus we use a commercial numerical solver, ABAQUS/STANDARD, for the numerical analyses. The built-in implicit solver uses Hilber-Hughes-Taylor method [3], but the numerical solution parameter α is set to zero so that the method becomes equivalent to the standard Newmark method. Design A and its variations are simulated for 30 s with the fixed time step $\Delta t = 10^{-5}$ s, and the frequency contents are obtained from the time responses between 10 and 30 s. Design B and its variations are simulated for 6 s with $\Delta t = 10^{-6}$ s, and the frequency contents are obtained from the response between 4 and 6 s. Design C is simulated for 20 s with $\Delta t = 10^{-5}$ s, and the frequency contents are obtained from the response between 10 and 20 s. Design D is simulated for 8 s with $\Delta t = 10^{-6}$ s, and the frequency contents are obtained from the response between 4 and 8 s.

$$\begin{aligned}&m_1\ddot{u}_{1,n}+\gamma m_1\dot{u}_{1,n}+\frac{k_2\left(-u_{1,n}+u_{2,n}+R\right)\left(\sqrt{L_2^2+R^2}-\sqrt{\left(-w_{1,n}+w_{2,n}+L_2\right)^2+\left(-u_{1,n}+u_{2,n}+R\right)^2}\right)}{\sqrt{\left(-w_{1,n}+w_{2,n}+L_2\right)^2+\left(-u_{1,n}+u_{2,n}+R\right)^2}}\\ &+\frac{k_3\left(-u_{1,n}+u_{3,n}+R\right)\left(\sqrt{L_3^2+R^2}-\sqrt{\left(w_{1,n}-w_{3,n}+L_3\right)^2+\left(-u_{1,n}+u_{3,n}+R\right)^2}\right)}{\sqrt{\left(w_{1,n}-w_{3,n}+L_3\right)^2+\left(-u_{1,n}+u_{3,n}+R\right)^2}}\\ &+\frac{k_1\left(-u_{1,n\text{-}1}+u_{1,n}+L_1\right)\left(\sqrt{\left(-u_{1,n\text{-}1}+u_{1,n}+L_1\right)^2+\left(w_{1,n\text{-}1}-w_{1,n}\right)^2}-L_1\right)}{\sqrt{\left(-u_{1,n\text{-}1}+u_{1,n}+L_1\right)^2+\left(w_{1,n\text{-}1}-w_{1,n}\right)^2}}\\ &-\frac{k_1\left(-u_{1,n}+u_{1,n+1}+L_1\right)\left(\sqrt{\left(-u_{1,n}+u_{1,n+1}+L_1\right)^2+\left(w_{1,n}-w_{1,n+1}\right)^2}-L_1\right)}{\sqrt{\left(-u_{1,n}+u_{1,n+1}+L_1\right)^2+\left(w_{1,n}-w_{1,n+1}\right)^2}}=0,\end{aligned} \tag{S.10}$$

$$
\begin{aligned}
&m_1\ddot{w}_{1,n}+\gamma m_1\dot{w}_{1,n}+\frac{k_2\left(-w_{1,n}+w_{2,n}+L_2\right)\left(\sqrt{L_2^2+R^2}-\sqrt{\left(-w_{1,n}+w_{2,n}+L_2\right)^2+\left(-u_{1,n}+u_{2,n}+R\right)^2}\right)}{\sqrt{\left(-w_{1,n}+w_{2,n}+L_2\right)^2+\left(-u_{1,n}+u_{2,n}+R\right)^2}}\\
&+\frac{k_3\left(w_{1,n}-w_{3,n}+L_3\right)\left(\sqrt{\left(w_{1,n}-w_{3,n}+L_3\right)^2+\left(-u_{1,n}+u_{3,n}+R\right)^2}-\sqrt{L_3^2+R^2}\right)}{\sqrt{\left(w_{1,n}-w_{3,n}+L_3\right)^2+\left(-u_{1,n}+u_{3,n}+R\right)^2}}\\
&+\frac{k_1\left(w_{1,n}-w_{1,n\text{-}1}\right)\left(\sqrt{\left(-u_{1,n\text{-}1}+u_{1,n}+L_1\right)^2+\left(w_{1,n\text{-}1}-w_{1,n}\right)^2}-L_1\right)}{\sqrt{\left(-u_{1,n\text{-}1}+u_{1,n}+L_1\right)^2+\left(w_{1,n\text{-}1}-w_{1,n}\right)^2}}\\
&+\frac{k_1\left(w_{1,n}-w_{1,n+1}\right)\left(\sqrt{\left(-u_{1,n}+u_{1,n+1}+L_1\right)^2+\left(w_{1,n}-w_{1,n+1}\right)^2}-L_1\right)}{\sqrt{\left(-u_{1,n}+u_{1,n+1}+L_1\right)^2+\left(w_{1,n}-w_{1,n+1}\right)^2}}=0,
\end{aligned}
\tag{S.11}
$$

$$
\begin{aligned}
&m_2\ddot{u}_{2,n}+\gamma m_2\dot{u}_{2,n}+\frac{k_2\left(-u_{1,n}+u_{2,n}+R\right)\left(\sqrt{\left(-w_{1,n}+w_{2,n}+L_2\right)^2+\left(-u_{1,n}+u_{2,n}+R\right)^2}-\sqrt{L_2^2+R^2}\right)}{\sqrt{\left(-w_{1,n}+w_{2,n}+L_2\right)^2+\left(-u_{1,n}+u_{2,n}+R\right)^2}}\\
&+\frac{k_4\left(-u_{2,n\text{-}1}+u_{2,n}+L_1\right)\left(\sqrt{\left(-u_{2,n\text{-}1}+u_{2,n}+L_1\right)^2+\left(w_{2,n\text{-}1}-w_{2,n}\right)^2}-L_1\right)}{\sqrt{\left(-u_{2,n\text{-}1}+u_{2,n}+L_1\right)^2+\left(w_{2,n\text{-}1}-w_{2,n}\right)^2}}\\
&-\frac{k_4\left(-u_{2,n}+u_{2,n+1}+L_1\right)\left(\sqrt{\left(-u_{2,n}+u_{2,n+1}+L_1\right)^2+\left(w_{2,n}-w_{2,n+1}\right)^2}-L_1\right)}{\sqrt{\left(-u_{2,n}+u_{2,n+1}+L_1\right)^2+\left(w_{2,n}-w_{2,n+1}\right)^2}}\\
&+\frac{k_7\left(u_{2,n}-u_{3,n\text{-}1}+L_1\right)\left(\sqrt{\left(u_{2,n}-u_{3,n\text{-}1}+L_1\right)^2+\left(w_{2,n}-w_{3,n\text{-}1}+L_2+L_3\right)^2}-\sqrt{L_1^2+\left(L_2+L_3\right)^2}\right)}{\sqrt{\left(u_{2,n}-u_{3,n\text{-}1}+L_1\right)^2+\left(w_{2,n}-w_{3,n\text{-}1}+L_2+L_3\right)^2}}\\
&+\frac{k_6\left(u_{2,n}-u_{3,n}\right)\left(\sqrt{\left(w_{2,n}-w_{3,n}+L_2+L_3\right)^2+\left(u_{2,n}-u_{3,n}\right)^2}-L_2-L_3\right)}{\sqrt{\left(w_{2,n}-w_{3,n}+L_2+L_3\right)^2+\left(u_{2,n}-u_{3,n}\right)^2}}\\
&-\frac{k_8\left(-u_{2,n}+u_{3,n+1}+L_1\right)\left(\sqrt{\left(-u_{2,n}+u_{3,n+1}+L_1\right)^2+\left(w_{2,n}-w_{3,n+1}+L_2+L_3\right)^2}-\sqrt{L_1^2+\left(L_2+L_3\right)^2}\right)}{\sqrt{\left(-u_{2,n}+u_{3,n+1}+L_1\right)^2+\left(w_{2,n}-w_{3,n+1}+L_2+L_3\right)^2}}=0,
\end{aligned}
\tag{S.12}
$$

$$
\begin{aligned}
&m_2\ddot{w}_{2,n}+\gamma m_2\dot{w}_{2,n}+\frac{k_2\left(-w_{1,n}+w_{2,n}+L_2\right)\left(\sqrt{\left(-w_{1,n}+w_{2,n}+L_2\right)^2+\left(-u_{1,n}+u_{2,n}+R\right)^2}-\sqrt{L_2^2+R^2}\right)}{\sqrt{\left(-w_{1,n}+w_{2,n}+L_2\right)^2+\left(-u_{1,n}+u_{2,n}+R\right)^2}}\\
&+\frac{k_4\left(w_{2,n}-w_{2,n\text{-}1}\right)\left(\sqrt{\left(-u_{2,n\text{-}1}+u_{2,n}+L_1\right)^2+\left(w_{2,n\text{-}1}-w_{2,n}\right)^2}-L_1\right)}{\sqrt{\left(-u_{2,n\text{-}1}+u_{2,n}+L_1\right)^2+\left(w_{2,n\text{-}1}-w_{2,n}\right)^2}}\\
&+\frac{k_4\left(w_{2,n}-w_{2,n+1}\right)\left(\sqrt{\left(-u_{2,n}+u_{2,n+1}+L_1\right)^2+\left(w_{2,n}-w_{2,n+1}\right)^2}-L_1\right)}{\sqrt{\left(-u_{2,n}+u_{2,n+1}+L_1\right)^2+\left(w_{2,n}-w_{2,n+1}\right)^2}}\\
&+\frac{k_7\left(w_{2,n}-w_{3,n\text{-}1}+L_2+L_3\right)\left(\sqrt{\left(u_{2,n}-u_{3,n\text{-}1}+L_1\right)^2+\left(w_{2,n}-w_{3,n\text{-}1}+L_2+L_3\right)^2}-\sqrt{L_1^2+\left(L_2+L_3\right)^2}\right)}{\sqrt{\left(u_{2,n}-u_{3,n\text{-}1}+L_1\right)^2+\left(w_{2,n}-w_{3,n\text{-}1}+L_2+L_3\right)^2}}\\
&+\frac{k_6\left(w_{2,n}-w_{3,n}+L_2+L_3\right)\left(\sqrt{\left(w_{2,n}-w_{3,n}+L_2+L_3\right)^2+\left(u_{2,n}-u_{3,n}\right)^2}-L_2-L_3\right)}{\sqrt{\left(w_{2,n}-w_{3,n}+L_2+L_3\right)^2+\left(u_{2,n}-u_{3,n}\right)^2}}\\
&+\frac{k_8\left(w_{2,n}-w_{3,n+1}+L_2+L_3\right)\left(\sqrt{\left(-u_{2,n}+u_{3,n+1}+L_1\right)^2+\left(w_{2,n}-w_{3,n+1}+L_2+L_3\right)^2}-\sqrt{L_1^2+\left(L_2+L_3\right)^2}\right)}{\sqrt{\left(-u_{2,n}+u_{3,n+1}+L_1\right)^2+\left(w_{2,n}-w_{3,n+1}+L_2+L_3\right)^2}}=0,
\end{aligned}
\tag{S.13}
$$

$$
\begin{aligned}
&m_3\ddot{u}_{3,n}+\gamma m_3\dot{u}_{3,n}+\frac{k_3\left(-u_{1,n}+u_{3,n}+R\right)\left(\sqrt{\left(w_{1,n}-w_{3,n}+L_3\right)^2+\left(-u_{1,n}+u_{3,n}+R\right)^2}-\sqrt{L_3^2+R^2}\right)}{\sqrt{\left(w_{1,n}-w_{3,n}+L_3\right)^2+\left(-u_{1,n}+u_{3,n}+R\right)^2}}\\
&+\frac{k_8\left(-u_{2,n\text{-}1}+u_{3,n}+L_1\right)\left(\sqrt{\left(-u_{2,n\text{-}1}+u_{3,n}+L_1\right)^2+\left(w_{2,n\text{-}1}-w_{3,n}+L_2+L_3\right)^2}-\sqrt{L_1^2+\left(L_2+L_3\right)^2}\right)}{\sqrt{\left(-u_{2,n\text{-}1}+u_{3,n}+L_1\right)^2+\left(w_{2,n\text{-}1}-w_{3,n}+L_2+L_3\right)^2}}\\
&-\frac{k_6\left(u_{2,n}-u_{3,n}\right)\left(\sqrt{\left(w_{2,n}-w_{3,n}+L_2+L_3\right)^2+\left(u_{2,n}-u_{3,n}\right)^2}-L_2-L_3\right)}{\sqrt{\left(w_{2,n}-w_{3,n}+L_2+L_3\right)^2+\left(u_{2,n}-u_{3,n}\right)^2}}\\
&-\frac{k_7\left(u_{2,n+1}-u_{3,n}+L_1\right)\left(\sqrt{\left(u_{2,n+1}-u_{3,n}+L_1\right)^2+\left(w_{2,n+1}-w_{3,n}+L_2+L_3\right)^2}-\sqrt{L_1^2+\left(L_2+L_3\right)^2}\right)}{\sqrt{\left(u_{2,n+1}-u_{3,n}+L_1\right)^2+\left(w_{2,n+1}-w_{3,n}+L_2+L_3\right)^2}}\\
&+\frac{k_5\left(-u_{3,n\text{-}1}+u_{3,n}+L_1\right)\left(\sqrt{\left(-u_{3,n\text{-}1}+u_{3,n}+L_1\right)^2+\left(w_{3,n\text{-}1}-w_{3,n}\right)^2}-L_1\right)}{\sqrt{\left(-u_{3,n\text{-}1}+u_{3,n}+L_1\right)^2+\left(w_{3,n\text{-}1}-w_{3,n}\right)^2}}\\
&-\frac{k_5\left(-u_{3,n}+u_{3,n+1}+L_1\right)\left(\sqrt{\left(-u_{3,n}+u_{3,n+1}+L_1\right)^2+\left(w_{3,n}-w_{3,n+1}\right)^2}-L_1\right)}{\sqrt{\left(-u_{3,n}+u_{3,n+1}+L_1\right)^2+\left(w_{3,n}-w_{3,n+1}\right)^2}}=0,
\end{aligned}
\tag{S.14}
$$

$$
\begin{aligned}
&m_3\ddot{w}_{3,n}+\gamma m_3\dot{w}_{3,n}+\frac{k_3\left(w_{1,n}-w_{3,n}+L_3\right)\left(\sqrt{L_3^2+R^2}-\sqrt{\left(w_{1,n}-w_{3,n}+L_3\right)^2+\left(-u_{1,n}+u_{3,n}+R\right)^2}\right)}{\sqrt{\left(w_{1,n}-w_{3,n}+L_3\right)^2+\left(-u_{1,n}+u_{3,n}+R\right)^2}}\\
&-\frac{k_8\left(w_{2,n\text{-}1}-w_{3,n}+L_2+L_3\right)\left(\sqrt{\left(-u_{2,n\text{-}1}+u_{3,n}+L_1\right)^2+\left(w_{2,n\text{-}1}-w_{3,n}+L_2+L_3\right)^2}-\sqrt{L_1^2+\left(L_2+L_3\right)^2}\right)}{\sqrt{\left(-u_{2,n\text{-}1}+u_{3,n}+L_1\right)^2+\left(w_{2,n\text{-}1}-w_{3,n}+L_2+L_3\right)^2}}\\
&-\frac{k_6\left(w_{2,n}-w_{3,n}+L_2+L_3\right)\left(\sqrt{\left(w_{2,n}-w_{3,n}+L_2+L_3\right)^2+\left(u_{2,n}-u_{3,n}\right)^2}-L_2-L_3\right)}{\sqrt{\left(w_{2,n}-w_{3,n}+L_2+L_3\right)^2+\left(u_{2,n}-u_{3,n}\right)^2}}\\
&-\frac{k_7\left(w_{2,n+1}-w_{3,n}+L_2+L_3\right)\left(\sqrt{\left(u_{2,n+1}-u_{3,n}+L_1\right)^2+\left(w_{2,n+1}-w_{3,n}+L_2+L_3\right)^2}-\sqrt{L_1^2+\left(L_2+L_3\right)^2}\right)}{\sqrt{\left(u_{2,n+1}-u_{3,n}+L_1\right)^2+\left(w_{2,n+1}-w_{3,n}+L_2+L_3\right)^2}}\\
&+\frac{k_5\left(w_{3,n}-w_{3,n\text{-}1}\right)\left(\sqrt{\left(-u_{3,n\text{-}1}+u_{3,n}+L_1\right)^2+\left(w_{3,n\text{-}1}-w_{3,n}\right)^2}-L_1\right)}{\sqrt{\left(-u_{3,n\text{-}1}+u_{3,n}+L_1\right)^2+\left(w_{3,n\text{-}1}-w_{3,n}\right)^2}}\\
&+\frac{k_5\left(w_{3,n}-w_{3,n+1}\right)\left(\sqrt{\left(-u_{3,n}+u_{3,n+1}+L_1\right)^2+\left(w_{3,n}-w_{3,n+1}\right)^2}-L_1\right)}{\sqrt{\left(-u_{3,n}+u_{3,n+1}+L_1\right)^2+\left(w_{3,n}-w_{3,n+1}\right)^2}}=0.
\end{aligned}
\tag{S.15}
$$

12 Movie S1: Coupling between the in-plane and out-of-plane motions

Movie S1 illustrates how the in-plane and out-of-plane motions are coupled with each other. The first half (between 3 and 20 s) of the playback shows the excitation of the flexural motion upon the passage of a single transition wave (or topological soliton) in the numerical Design B. The responses in Y-direction (in the simulation coordinate) is scaled by 40 times to aid the identification of the out-of-plane motion visually. Similarly, the second half (between 25 and 46 s) of the playback shows the coupling in the experimental demonstrator.

13 Movie S2: Experimental demonstration

Movie S2 shows an experimental observation of solitonic resonance under 1.1 Hz displacement input large enough to trigger transition waves. As transition waves propagate within the metabeam, a series of free vibrations near the natural frequency of the structure occurs, yielding an output frequency contribution different from the input frequency. The solitonic resonance is manifested by the faster transverse vibration than the input frequency.

14 Movie S3: Solitonic resonance

Movie S3 shows simulations of solitonic resonance responses obtained under $F = 1.7$ N at 8 Hz, 36 Hz, and 68 Hz. The first half (starting at 3 s) of the playback shows the animated results between 4 and 5 s in the simulation time. Transition wave propagation within each metabeam is observable from the recurrent oscillations of the bistable elements between the stable points. To better identify the macroscopic structural motion, we scale the deformations by ten times for the second half (starting at 19 s) of the playback. The stable propagation of the compression and rarefaction wave groups bolsters the quasi-particle nature of the transition waves. Even though the input frequencies are drastically different, the out-of-plane motions occur at a similar frequency, indicating input-independent frequency conversion.

References

[1] T. Dauxois and M. Peyrard, *Physics of Solitons*. Cambridge University Press, 2006.

[2] M. Hwang and A. F. Arrieta, "Energy harvesting characteristics in metamaterials based on bistable lattices," in *Active and Passive Smart Structures and Integrated Systems XIII* (A. Erturk, ed.), SPIE, mar 2019.

[3] H. M. Hilber, T. J. R. Hughes, and R. L. Taylor, "Improved numerical dissipation for time integration algorithms in structural dynamics," *Earthquake Engineering & Structural Dynamics*, vol. 5, pp. 283–292, jul 1977.